Supporting information

In-situ topotactic formation of the inorganic intergrowth bulk heterojunction NiS/FeS@MgFe-LDHs to simulate the carbon monoxide dehydrogenase for photocatalytic reduction CO_2

Yuexian Li[a], Wenli Su[c], Xiaoyan Wang[a], Jun Lu[*a,b], Wenkai Zhang[*c], Shuo Wei[*d]

[a]State Key Laboratory of Chemical Resource Engineering and College of Chemistry, Beijing University of Chemical Technology, P. Box 98, Beisanhuan East Road 15, Beijing 100029, P. R. China.

[b]Beijing Advanced Innovation Center for Soft Matter Science and Engineering, Beijing University of Chemical Technology, P. Box 98, Beisanhuan East Road 15, Beijing 100029, P. R. China.

[c]Department of Physics and Applied Optics Beijing Area Major Laboratory, Center for Advanced Quantum Studies, Beijing Normal University, Xinjiekou Outside Street 19, Beijing 100875, China

[d]College of Chemistry, Beijing Normal University, Xinjiekou Outside Street 19, Beijing 100875, P. R. China

*E-mail (J. Lu): lujun@mail.buct.edu.cn *E-mail (W.K. Zhang): wkzhang@bnu.edu.cn *E-mail (S. Wei): vshuo@bnu.edu.cn

1. Characterization

2. Table and Fig.

Fig. S7. GC standard curve for the quantitative determination of pure **(A)** CO and **(B)** CH_4 by external standard method. **(C)** The isotope experiments of photocatalytic CO_2 methanation with $^{13}CO_2$.

Fig. S8. (A) Photocatalytic blank and control experiments. **(B)** Photocatalytic experiments with catalysts obtained at different vulcanisation times. **(C)** The *in-situ* FTIR of the NiMgFe-LDHs.

Fig. S9. The XRD pattern of the IIBH NiS/FeS@MgFe-LDHs underwent the photocatalytic reduction CO_2.

Fig. S10. The XPS spectra of of NiMgFe-LDHs, NiMgFe-MMO, and of NiS/FeS@MgFe-LDHs **(A)** Fe 2p; **(B)** Ni 2p; **(C)** S 2p; **(D)** O1s. **(E)** S 2p of NiS/FeS@MgFe-LDHs, FeS and NiS. The ISI-XPS of **(F)** FeS; **(G)** NiS; **(H)** Mg 1s of NiS/FeS@MgFe-LDHs; **(I)** S 2p of NiS/FeS@MgFe-LDHs.

Fig. S11. The TAS spectra of (A) NiMgFe-LDHs; (B) FeS; (C) NiS+FeS mixture in CH_3OH at 350nm excitaion.

1. Characterization.

Powder X-ray diffraction (XRD) using Cu K radiation (λ = 0.154 nm, 40 kV, and 40 mA) on the Rigaku UItima III diffractometer was used to explore crystal structure identification. The scan speed was 10° min^{-1}, and the 2theta range was 5° to 70°. Transmission electron microscopy (TEM, JEM-3010) and scanning electron microscopy (SEM, Zeiss) were used for analyzing the morphology of the photocatalysts. Using a Hitachi U-3900H spectrophotometer and white $BaSO_4$ as the reflection standard, UV-Visible diffuse reflectometry (UV-DRS) was used to examine the photocatalyst's light absorption characteristics. The functional group of the materials was identified using the Fourier transform infrared spectrometer (FT-IR, TENSOR II). Utilizing a Thermo Fisher Scientific ESCALAB 250, X-ray photoelectron spectroscopy (XPS) examination was carried out, and Al Kα = 1486 eV radiation was employed to investigate the surface composition and chemical valence states. Similar circumstances were used for in-situ irradiation XPS measurements, however UV-visible light irradiation was added. The HITACHIF-4600 fluorescence spectrophotometer was used to examine the PL spectra of each sample. The femtosecond transient absorption spectra (fs-TAS) were recorded using Helios equipment, and the nondegenerate pump-probe system was utilized to look at the dynamics of transients from 0.5 picoseconds to 200 picoseconds. The 350 nm-pump pulses (5 mW on average at the tested samples) were created by the O PerA Solo optical parametric amplifier (Coherent Libra, 800 nm, 50 fs, 4 mJ), and they were pumped by an LBO laser (Coherent Evolution-50C, 1 kHz system). A mode-locked Ti-sapphire oscillator (Coherent Vitesse, 80 MHz) was used to seed the amplifier. The white light continuum from 475 nm to 850 nm was created by forcing the 800 nm-femtosecond pluses through a constantly rotating CaF2 crystal. The Beijing Synchrotron Radiation Facility (BSRF) used the 1W1B beamline and a double crystal Si (111) monochromator to produce X-ray absorption fine structure (XAFS) investigations.

Electrochemical testing. The electrochemical workstation (CHI660E) with a three-electrode setup and a spinning ring disk was used for the electrochemical impedance spectroscopy (EIS) testing. The electrolyte was pH = 6.8, 0.1 M Na_2SO_4 aqueous solution. The reference electrode and counter electrode were Hg/Hg_2Cl_2 and graphite electrode, respectively. In 485 μL of deionized water and 485 μL of ethanol, 10 mg of various catalyst samples were scattered with 30 μL of nafion as adhesive. The samples were uniformly deposited on a glassy carbon

electrode after an ultrasonic dispersion period of 10 min. Without applying bias voltage, the photocurrent response was utilized to measure the current produced by the sample in either bright or dark conditions. Using the Mott-Schottky plot, the flat band potential (V_{fb}) in the semiconductor space charge area was computed.

Photocatalytic reduction of CO_2 experiment. In a 100 mL quartz photocatalytic reaction cell, 30 mg of photocatalysts were dissolved in 35 mL of deionized water using an ultrasonic dispersion technique for 10 minutes. The reaction cell was then cycled with CO_2 pure gas for 30 minutes. In order to reduce CO_2 and keep the entire photocatalytic system at room temperature, a 300 mW/cm^2 xenon lamp was employed. Gas chromatography (GC-7920, TDX-01 packed column) with a flame ionization detector (FID) as N_2 carrier gas was used to monitor the gas products. For each catalyst, at least three parallel tests were conducted to guarantee the correctness of the photocatalytic test data.

***In-situ* fourier transform infrared spectroscopy on CO_2 reaction experiment.** The BaF_2 window and MCT detector were installed in the Nicolet 6700 *in-situ* fourier transform infrared spectrometer. The device has a measuring range of 4000 to 400 cm^{-1}. The measuring mode employed was diffuse reflection. First, CO_2 and H_2O that had been adsorbed on the catalyst's surface were removed using high-pure He. The *in-situ* spectroscopic cell was filled with the photocatalyst, He gas was continually added, and the temperature was controlled to rise from ambient temperature to 100 ℃ at a rate of 10 ℃/minute for 40 min. At room temperature, blank background data was gathered before high-purity CO_2 and water vapor were bubbled into the *in-situ* spectroscopic cell. CO_2 gas flowed at a rate of 10 ml/min. To produce the spectra of the CO_2 reaction after the various illumination times, the spectra were taken at intervals of 2 min and exposed to radiation for 30 min. Condensing the flowing water and maintaining room temperature in the *in-situ* spectroscopic cell allowed the entire reaction to be carried out.

Table S1. Local structure parameters around Fe estimated by EXAFS analysis.

Sample	Shell	S_0^2N[a]	R[Å][b]	σ^2[10^{-3}Å^2][c]	ΔE_0	R-factor (10^{-3})
NiMgFe-LDHs	Fe-O	6.0	1.42 ± 0.01	5.31	0.3	10.01
	Fe-O-M[d]	6.0	2.46 ± 0.01	4.73	0.2	
NiMgFe-MMO	Fe-O	5.99	1.41 ± 0.01	5.22	-1.5	11.35
	Fe-O-M	5.97	2.44 ± 0.01	5.12	-0.1	
NiS/FeS@MgFe-LDHs	Fe-S	6.0	1.49 ± 0.01	6.91	0.5	11.69
	Fe-O-M	5.99	2.46 ± 0.01	4.37	1.3	
	Fe-S-M	5.81	3.01 ± 0.01	5.02	1.1	

[a] N: coordination number; [b] R: distance between adsorber and backscatter atoms; [c] σ^2: Debye-Waller factor; [d] M: Fe or Ni.

We known that the basic single scattering formula of EXAFS can be written in the following form：[1]

$$\chi(k) = \sum_j N_j S_0^2 F_j(k) \cdot \frac{1}{kR_j^2} \cdot e^{-2\sigma_j^2 k^2} \cdot e^{-2R_j/\lambda(k)} \cdot sin[2kR_j + \phi_j^l(k)]$$

Among them, the physical quantity N_j and R_j has been discussed above, and the Debye-Waller factor σ^2 is also worth paying attention to, which is related to the disorder in the system. The so-called disorder is the

scattering atom position deviates from R_j, and this deviation will cause the absorption peak to broaden,[2] which included thermal disorder caused by thermal vibration and structural disorder brought by structural distortion ($\sigma^2 = \sigma^2_T + \sigma^2_S$).[1] Under the same test conditions of temperature, the variation of σ^2 might partially account for the the disorder of crystal structure in atomic size.

Table S2. Local structure parameters around Ni estimated by EXAFS analysis.

Sample	Shell	N[a]	R[Å][b]	σ^2[10^{-3}Å^2][c]	ΔE_0	R-factor (10^{-3})
NiMgFe-LDHs	Ni-O	6.0	1.58 ± 0.01	5.21	-0.6	10.05
	Ni-O-M[d]	6.0	2.63 ± 0.01	6.37	1.1	
NiMgFe-MMO	Ni-O	5.9	1.56 ± 0.01	5.58	-1.3	10.79
	Ni-O-Ni	5.7	2.51 ± 0.01	6.70	1.7	
NiS/FeS@MgFe-LDHs	Ni-S	5.3	1.61 ± 0.01	6.35	-0.1	8.57
	Ni-S-M	5.1	2.47 ± 0.01	5.41	1.3	

[a] N: coordination number; [b] R: distance between adsorber and backscatter atoms; [c] σ^2: Debye-Waller factor; [d] M: Ni or Fe.

Table S3. Photocatalytic test results for the systems irradiated by UV-vis light for 5 h.

photocatalyst	The yields of CO (μmol/g·h)	The yields of CH_4 (μmol/g·h)	TCEN[a] (μmol/mg)	Activity improvement rate[b] (%)	Apparent quantum yield [c] (AQY, %)	CO Selectivity[d] S (%)
NiMgFe-LDHs	54.0189	5.4077	4.2433	0	1.8715	71.4%
NiMgFe-MMO	221.6183	22.663	20.8180	45.9167	5.0871	70.9.%
NiS/FeS@MgFe-LDHs	2151.974	108.563	199.0817	-	14.7146	83.2%
Pure NiS	24.1119	2.1378	2.1775	-	0.0734	73.8%
Pure FeS	20.0218	2.6123	2.0314	0.8668	0.1379	65.7%
NiS + FeS mixture	60.6731	14.537	7.9214	3.9061	1.3602	51.1%

The potoreduction CO_2 results can be calculation by equation below:

$$[a]\ \mathrm{TCEN} = \frac{\sum(n_{\mathrm{production}} \times n_{\mathrm{electrons}})}{m_{\mathrm{cat.}}}$$

TCEN was represented the total number of electrons actually consumed in photocatalytic CO_2 reduction, $n_{production}$ and $n_{electrons}$ were the yields of actual product of CO_2 reduction and the moles of electrons reacted to form a mole product (CO: $n_{electrions} = 2$; CH_4: $n_{electrions} = 8$), respectively.

The $n_{(CH4)}$ and $n_{(CO)}$ represented the yields of CH_4 and CO.

$$[b]\ \text{Activity improvement rate}\ (\%) = \frac{\mathrm{TCEN}_{(\mathrm{catalysts})} - \mathrm{TCEN}_{(\mathrm{CuNiAl-LDH})}}{\mathrm{TCEN}_{(\mathrm{CuNiAl-LDH})}} \times 100\%$$

$$[c]\ AQY = \frac{CH_4\ yields\ (\mu mol/s) \times 8 + CO\ yields\ (\mu mol/s) \times 2}{Photon\ flux\ (\mu mol/s)} \times 100\%$$

where, both, yields of products and photon intensity are in μmol. Photon intensity can be calculated as follow:[3]

$$Photon\ flux\ (\mu mol/s) = \frac{Intensity\ of\ light\ \times Wavelength}{Planck\ constant\ \times Photon\ density} \times \frac{Incident\ area}{Avogadro's\ constant}$$

The intensity of the lamp is represented in Wm^{-2}, the light wavelength is in meters (m) and the reactor incident area is calculated in m^2. Planck's constant, Photondensity, and Avogadro's number are with values 6.63×10^{-34} J·s, 3×10^8 m·s^{-1}, and 6.63×10^{23} mol^{-1}, respectively.

[d] $$S = \frac{CO\ yields\ (\mu mol/gh) \times 2}{CO\ yields\ (\mu mol/gh) \times 2 + CH4\ yields\ (\mu mol/gh)} \times 100\%$$

Table S4. The photocatalytic performance comparison of CO_2 reduction over various catalysts.

photocatalyst	mass	Energy source	Hydrogen source	CO production	CH_4 production	Ref.
NiS/FeS@MgFe-LDHs	30mg	Xenon lamp of 300 mW·cm^{-2}	H_2O	2151.974 μmol/g_{cat}·h	108.563 μmol/g_{cat}·h	This work
$FeNi_2S_4$	30mg	electroreduction -0.8 V	H_2O	-	-	[4]
CODH/AgNCs-PMAA	5mg	300 W arc lamp with 420 nm filter	H_2O	11.36 μmol/g_{cat}·h	-	[5]
Ni-2,6-bis([(2-pyridinylmethyl)thio]methyl) pyridine)	30mg	300 W Xenon lamp (λ > 420 nm)	H_2O	25 μmol/g_{cat}·h	-	[6]
poly(2-(dimethylamino)ethyl methacrylate)	0.1g	300 W Xenon lamp (λ > 420 nm)	H_2O	2.2 μmol/g_{cat}·h	-	[7]
CODH-DIH	30mg	300 W Xenon lamp	H_2O	1.77 μmol/g_{cat}·h	-	[8]
TiO_2-CODH	50mg	300 W Xenon lamp (λ > 420 nm)	H_2O	250 μmol/g_{cat}·h	11.8 μmol/g_{cat}·h	[9]

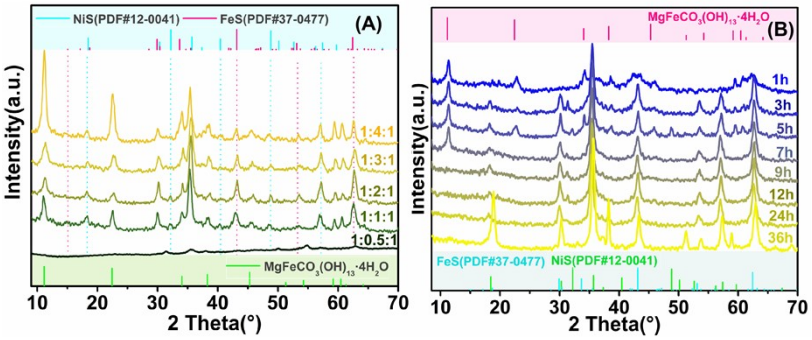

Fig. S1. The XRD of **(A)** the different molar ratios of NiMgFe-LDHs precursors to vulcanize. **(B)** NiMgFe-MMO at different vulcanizing time.

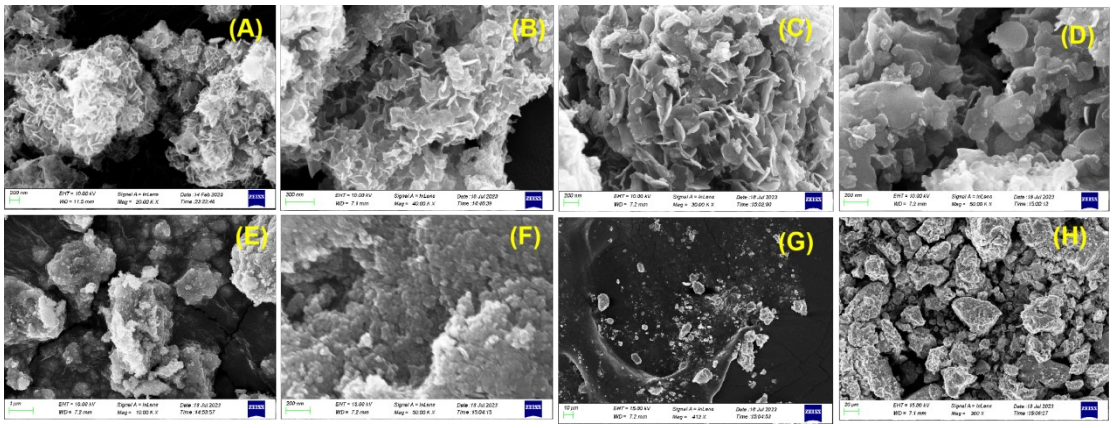

Fig. S2. The SEM images of NiMgFe-MMO at different vulcanizing time **(A)** 1h; **(B)** 3h; **(C)** 5h; **(D)** 7h; **(E)** 9h; **(F)** 12h; **(G)** 24h; **(H)** 36h.

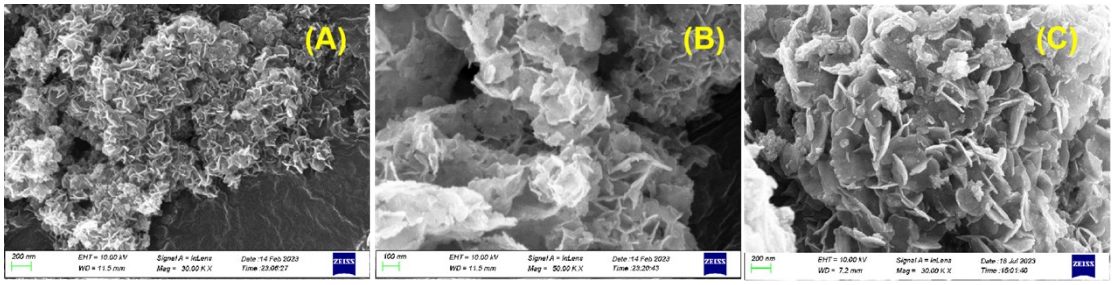

Fig. S3. The scanning electron microscope (SEM) images of catalysts **(A)** NiMgFe-LDHs; **(B)** NiMgFe-MMO; **(C)** NiS/FeS@MgFe-LDHs.

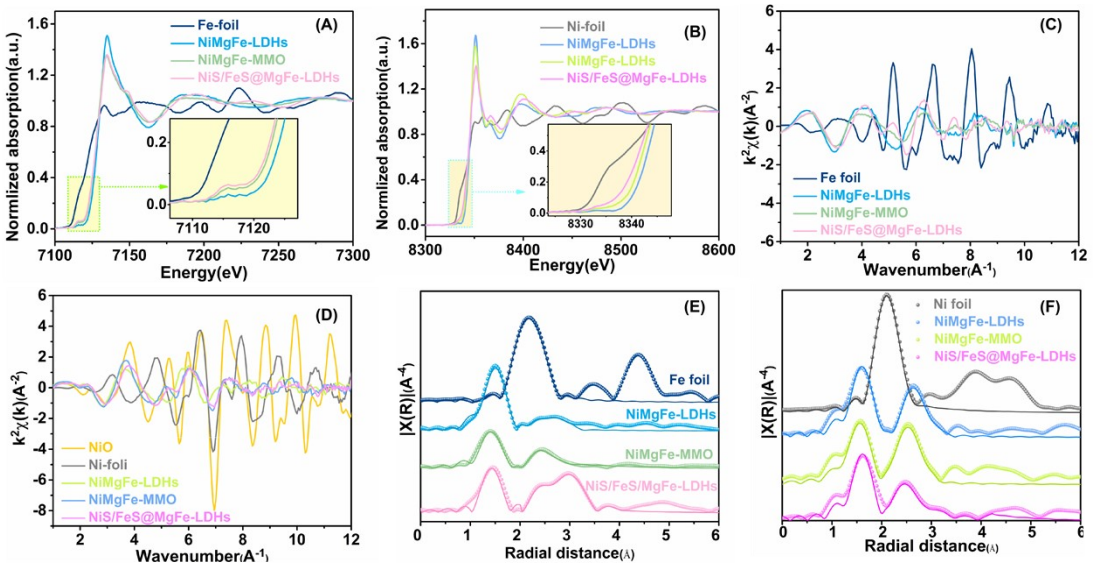

Fig. S4. K-edge of XAS for **(A)** Fe, **(B)** Ni. The oscillation function $k^3\chi(k)$ of the K-edge in XAS for **(C)** Fe, **(D)** Ni. The magnitude of k^3-weighted FT and corresponding fitting of K-edge for **(E)** Fe, **(F)** Ni.

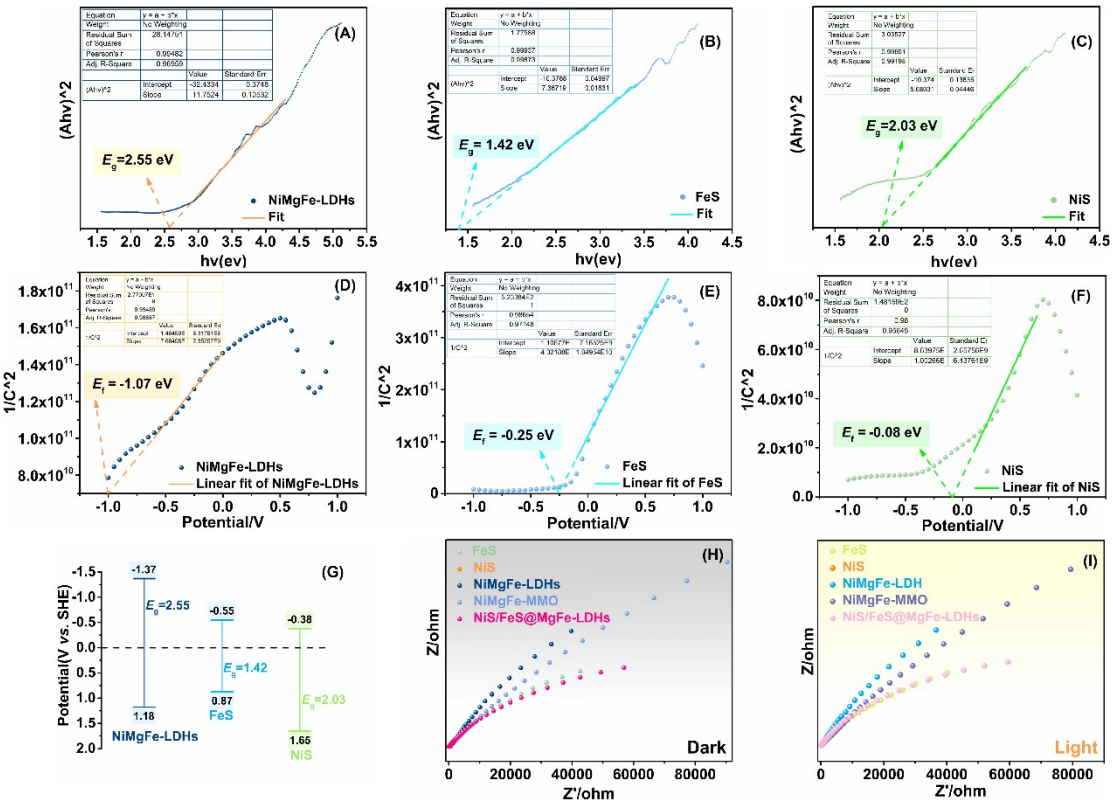

Fig. S5. **(A-C)** The UV-vis diffuse reflectance spectra were fitted with Kubelka-Munk formula and Tauc's plot to estimate the band gap. Mott-Schottky plot of the **(D)** NiMgFe-LDHs, **(E)** FeS, **(F)** NiS. **(G)** Schematic diagram of the location of the energy bands. **(H-I)** The EIS of the NiMgFe-LDHs, NiMgFe-MMO, FeS, NiS, and NiS/FeS@MgFe-LDHs in light and dark.

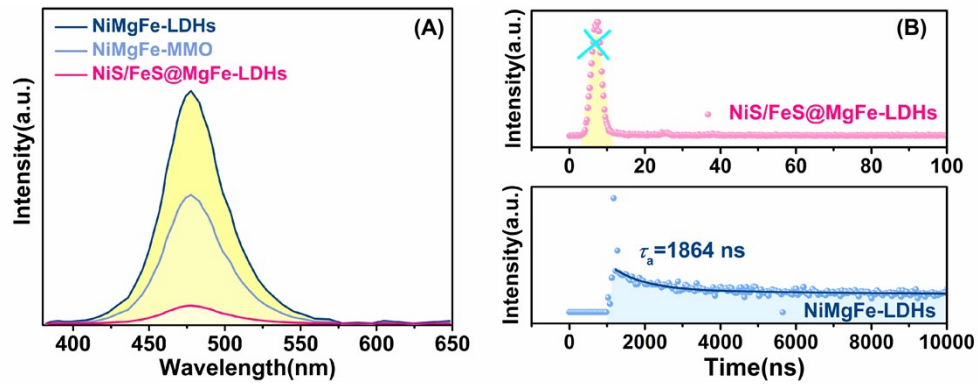

Fig. S6. **(A)** The photoluminescece spectra of all catalysts with 320 nm excitation. **(B)** TRPL spectra of NiMgFe-LDHs and IIBH NiS/FeS@MgFe-LDHs with 343 nm excitation and 470 nm emission.

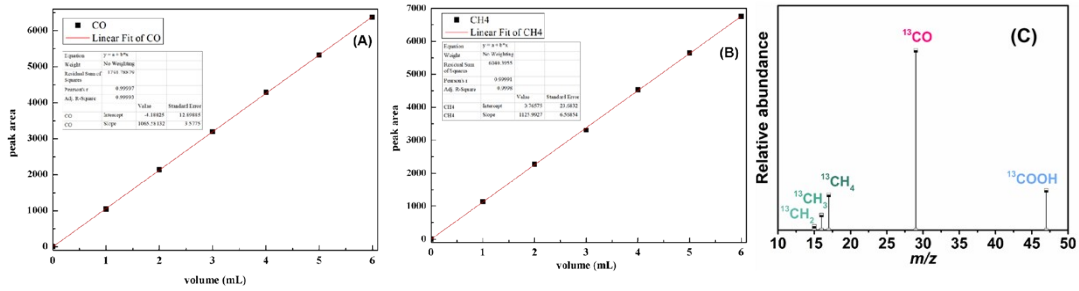

Fig. S7. GC standard curve for the quantitative determination of pure **(A)** CO and **(B)** CH_4 by external standard

method. **(C)** The isotope experiments of photocatalytic CO_2 methanation with $^{13}CO_2$.

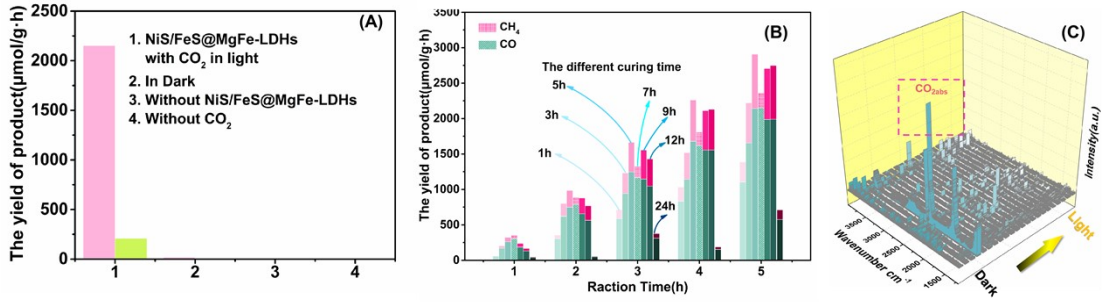

Fig. S8. (A) Photocatalytic blank and control experiments. **(B)** Photocatalytic experiments with catalysts obtained at different vulcanisation times. **(C)** The *in-situ* FTIR of the NiMgFe-LDHs.

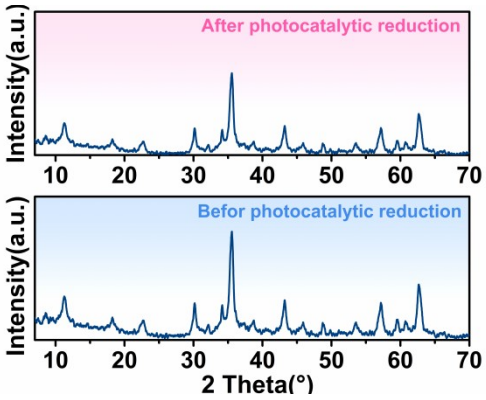

Fig. S9. The XRD pattern of the IIBH NiS/FeS@MgFe-LDHs underwent the photocatalytic reduction CO_2.

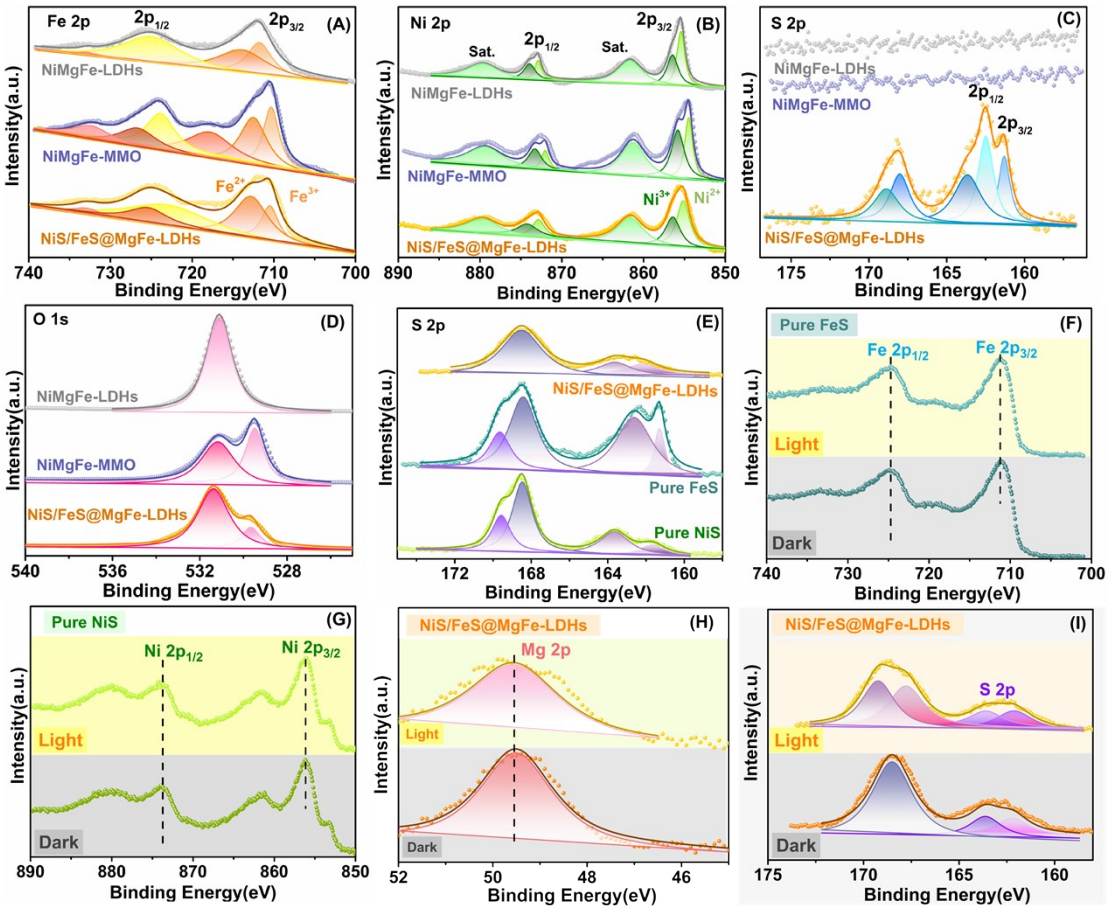

Fig. S10. The XPS spectra of of NiMgFe-LDHs, NiMgFe-MMO, and of NiS/FeS@MgFe-LDHs **(A)** Fe 2p; **(B)** Ni 2p; **(C)** S 2p; **(D)** O1s. **(E)** S 2p of NiS/FeS@MgFe-LDHs, FeS and NiS. The ISI-XPS of **(F)** FeS; **(G)** NiS; **(H)** Mg 1s of NiS/FeS@MgFe-LDHs; **(I)** S 2p of NiS/FeS@MgFe-LDHs.

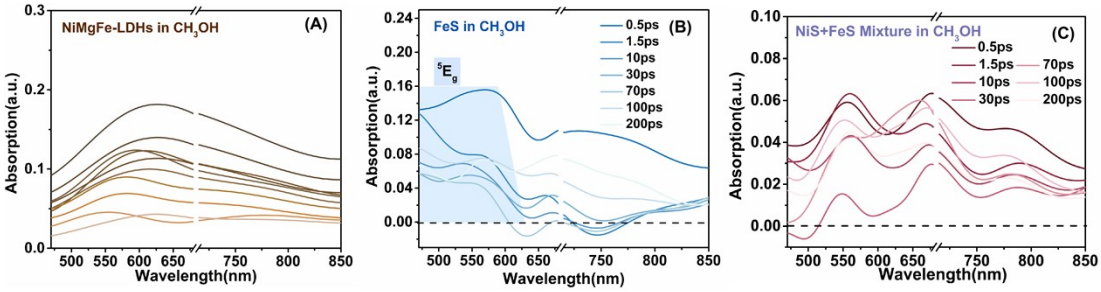

Fig. S11. The TAS spectra of **(A)** NiMgFe-LDHs; **(B)** FeS; **(C)** NiS+FeS mixture in CH_3OH at 350nm excitaion.

Reference:

1. B. Ravel and M. Newville, *Journal of Synchrotron Radiation*, 2005, **12**, 537-541.
2. P. Eisenberger and B. M. Kincaid, *Science*, 1978, **200**, 1441-1447.
3. H. Kumagai, Y. Tamaki and O. Ishitani, *Accounts of Chemical Research*, 2022, **55**, 978-990.
4. J.-E. Lee, A. Yamaguchi, H. Ooka, T. Kazami, M. Miyauchi, N. Kitadai and R. Nakamura, *Chemical Communications*, 2021, **57**, 3267-3270.
5. L. Zhang, M. Can, S. W. Ragsdale and F. A. Armstrong, *ACS Catalysis*, 2018, **8**, 2789-2795.
6. Q. He, B. Wu, Y. Hu, W. Huang and Y. Li, *Science China Chemistry*, 2020, **63**, 1716-1720.
7. H. Dai, R. Cui, C. Chen, J. Song, J. Li, L. Dong, C. Yu, W. Jiang and Y. Zhou, *Chemistry – A European Journal*, 2023, **29**, e202300879.
8. D. W. White, D. Esckilsen, S. K. Lee, S. W. Ragsdale and R. B. Dyer, *The Journal of Physical Chemistry Letters*, 2022, **13**, 5553-5556.
9. T. W. Woolerton, S. Sheard, E. Reisner, E. Pierce, S. W. Ragsdale and F. A. Armstrong, *Journal of the American Chemical Society*, 2010, **132**, 2132-2133.